On immunizing five-beta hybrid-stress element models from 'trapezoidal locking' in practical analyses

K. Y. Sze*

Department of Mechanical Engineering, The University of Hong Kong, Pokfulam Road, Hong Kong SAR, People's Republic of China

SUMMARY

When multiple trapezoidal four-node plane elements are used to model slender beams, it is found that the transverse bending stress/strain mode which should physically vanish is most detrimental to the element accuracy and leads to a deficiency which is sometimes known as 'trapezoidal locking'. In this paper, immunity of four-node five-beta hybrid elements to 'trapezoidal locking' in practical analyses is obtained by a simple selective scaling procedure that judiciously reduces the stiffness arising from the two bending stress/strain modes in the elements. Copyright © 2000 John Wiley & Sons, Ltd.

KEY WORDS: hybrid formulation; finite element; trapezoidal locking; selective scaling

1. INTRODUCTION

In the past three decades, tremendous efforts have been put into improving the accuracy of the four-node plane element. Advanced finite element techniques including hybrid/mixed method [1–6], incompatible displacement modes [7, 8], enhanced strain method [9], γ-stabilization method [10], selectively reduced integration (SRI) [11] and assumed strain formulation [12, 13] have been applied. Most, if not all, of the techniques have yielded finite element models with excellent accuracy in beam-bending problems when rectangular meshes are employed. Unless patch test fulfillment is sacrificed such as the elements presented in References 7 and 13, the element accuracy drops substantially if trapezoidal meshes are used. This deterioration is sometimes known as 'trapezoidal locking' [14, 15] and is one of the impetuses for developing four-node plane elements with Allman's drilling rotational d.o.f.s [16–20].

In this paper, the geometry and kinematics of the four-node element is first reviewed. Single-element tests are conducted and the most critical parasitic strain mode leading to 'trapezoidal locking' in practical analyses, where more than one element are employed, is identified to be the transverse bending mode which should physically vanish. Based on the finding, the five-beta hybrid-stress elements proposed by Pian and Sumihara [2] and Yuan *et al.* [4] are modified by

a devised selective scaling technique. The resulting elements pass the patch test and do not suffer from 'trapezoidal locking' in practical analyses.

2. FOUR-NODE QUADRILATERAL ELEMENT

Besides the rigid-body and constant-strain modes, the four-node element possesses two bending or, equivalently, hourglass deformation modes [10]. The two bending modes in beam analyses would here be termed as longitudinal and transverse bending modes when their bending strains are, respectively, essentially parallel and transverse to the applied bending stress as defined in Figure 1. For the element the global Cartesian co-ordinates and displacement interpolations in terms of the natural co-ordinates ξ and η are

$$x = \sum_{i=1}^{4} N_i x_i = a_0 + a_1 \xi + a_2 \xi \eta + a_3 \eta, \quad y = \sum_{i=1}^{4} N_i y_i = b_0 + b_1 \xi + b_2 \xi \eta + b_3 \eta \tag{1a}$$

$$u = \sum_{i=1}^{4} N_i u_i = [N_1, N_2, N_3, N_4] \mathbf{u}^e, \quad v = \sum_{i=1}^{4} N_i v_i = [N_1, N_2, N_3, N_4] \mathbf{v}^e \tag{1b}$$

where

$$N_1 = (1 - \xi)(1 - \eta)/4, \quad N_2 = (1 + \xi)(1 - \eta)/4$$

$$N_3 = (1 + \xi)(1 + \eta)/4, \quad N_4 = (1 + \xi)(1 - \eta)/4$$

(x_i, y_i) and (u_i, v_i) are the nodal co-ordinates and displacements of the ith node

$$\mathbf{u}^e = \{u_1, u_2, u_3, u_4\}^T, \quad \mathbf{v}^e = \{v_1, v_2, v_3, v_4\}^T,$$

$$\begin{bmatrix} a_0 & b_0 \\ a_1 & b_1 \\ a_2 & b_2 \\ a_3 & b_3 \end{bmatrix} = \frac{1}{4} \begin{bmatrix} +1 & +1 & +1 & +1 \\ -1 & +1 & +1 & -1 \\ +1 & -1 & +1 & -1 \\ -1 & -1 & +1 & +1 \end{bmatrix} \begin{bmatrix} x_1 & y_1 \\ x_2 & y_2 \\ x_3 & y_3 \\ x_4 & y_4 \end{bmatrix}$$
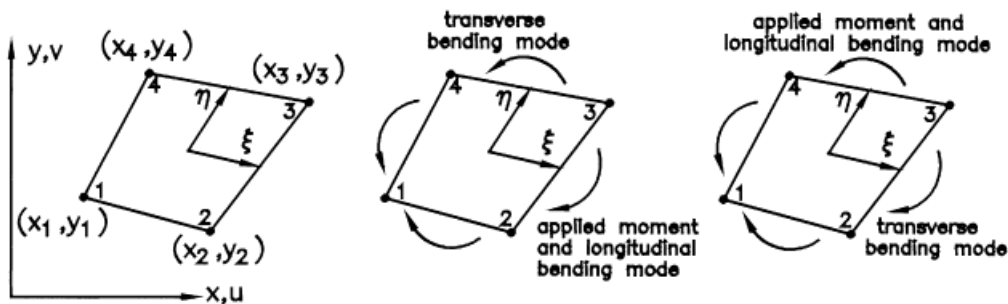

Figure 1. Four-node plane element and the definitions for longitudinal and transverse bending modes with respect to the applied moment

Moreover, the Jacobian determinant can be expressed as

$$j = \frac{\partial x}{\partial \xi}\frac{\partial y}{\partial \eta} - \frac{\partial x}{\partial \eta}\frac{\partial y}{\partial \xi} = j_0 + j_1\xi + j_2\eta = (a_1 b_3 - a_3 b_1) + (a_1 b_2 - a_2 b_1)\xi + (a_2 b_3 - a_3 b_2)\eta \quad (2)$$

Using the technique of expressing the displacement-derived strain in γ-stabilization method [10], the strain can be partitioned into the following constant constituent $\boldsymbol{\varepsilon}_c$ and non-constant constituent $\boldsymbol{\varepsilon}_{nc}$:

$$\boldsymbol{\varepsilon}_c = \left\{\begin{matrix} \varepsilon_x \\ \varepsilon_y \\ \gamma_{xy} \end{matrix}\right\}_c = \begin{bmatrix} \mathbf{b}_x & \mathbf{0} \\ \mathbf{0} & \mathbf{b}_y \\ \mathbf{b}_y & \mathbf{b}_x \end{bmatrix}\left\{\begin{matrix} \mathbf{u}^e \\ \mathbf{v}^e \end{matrix}\right\} = \mathbf{B}_c\left\{\begin{matrix} \mathbf{u}^e \\ \mathbf{v}^e \end{matrix}\right\}, \quad \boldsymbol{\varepsilon}_{nc} = \left\{\begin{matrix} \varepsilon_x \\ \varepsilon_y \\ \gamma_{xy} \end{matrix}\right\}_c = \begin{bmatrix} h_x\mathbf{g} & \mathbf{0} \\ \mathbf{0} & h_y\mathbf{g} \\ h_y\mathbf{g} & h_x\mathbf{g} \end{bmatrix}\left\{\begin{matrix} \mathbf{u}^e \\ \mathbf{v}^e \end{matrix}\right\} = \mathbf{B}_{nc}\left\{\begin{matrix} \mathbf{u}^e \\ \mathbf{v}^e \end{matrix}\right\} \quad (3)$$

where

$$\mathbf{b}_x = \frac{1}{4j_0}\left[\, +b_1 - b_3, \ +b_1 + b_3, \ -b_1 + b_3, \ -b_1 - b_3\,\right]$$

$$\mathbf{b}_y = \frac{1}{4j_0}\left[\, -a_1 + a_3, \ -a_1 - a_3, \ +a_1 - a_3, \ +a_1 + a_3\,\right]$$

$$\mathbf{g} = \frac{1}{4j_0}\left[\, +j_0 + j_1 + j_2, \ -j_0 + j_1 - j_2, \ +j_0 - j_1 - j_2, \ -j_0 - j_1 + j_2\,\right]$$

$$h_x = \frac{\partial(\xi\eta)}{\partial x} = \frac{1}{j}(b_3\eta - b_1\xi) \quad \text{and} \quad h_y = \frac{\partial(\xi\eta)}{\partial y} = \frac{1}{j}(a_1\xi - a_3\eta)$$

For the SRI element with reduced or single-point integration applied to the shear energy [11], the effective strain constituents are

$$\boldsymbol{\varepsilon}_c = \left\{\begin{matrix} \varepsilon_x \\ \varepsilon_y \\ \gamma_{xy} \end{matrix}\right\}_c = \begin{bmatrix} \mathbf{b}_x & \mathbf{0} \\ \mathbf{0} & \mathbf{b}_y \\ \mathbf{b}_y & \mathbf{b}_x \end{bmatrix}\left\{\begin{matrix} \mathbf{u}^e \\ \mathbf{v}^e \end{matrix}\right\} \quad \text{and} \quad \boldsymbol{\varepsilon}_{nc} = \left\{\begin{matrix} \varepsilon_x \\ \varepsilon_y \\ \gamma_{xy} \end{matrix}\right\}_c = \begin{bmatrix} h_x\mathbf{g} & \mathbf{0} \\ \mathbf{0} & h_y\mathbf{g} \\ \mathbf{0} & \mathbf{0} \end{bmatrix}\left\{\begin{matrix} \mathbf{u}^e \\ \mathbf{v}^e \end{matrix}\right\} \quad (4)$$

As the area integrals of h_x and h_y vanish, the stiffness matrix of the element can be written as

$$\mathbf{k}_{SRI} = \mathbf{k}_c + \mathbf{k}_{nc} \quad (5)$$

where

$$\mathbf{k}_c = 4j_0 \begin{bmatrix} \mathbf{b}_x & \mathbf{0} \\ \mathbf{0} & \mathbf{b}_y \\ \mathbf{b}_y & \mathbf{b}_x \end{bmatrix}^{\mathrm{T}} \mathbf{C} \begin{bmatrix} \mathbf{b}_x & \mathbf{0} \\ \mathbf{0} & \mathbf{b}_y \\ \mathbf{b}_y & \mathbf{b}_x \end{bmatrix} \quad \text{and} \quad \mathbf{k}_{nc} = \left\langle \begin{bmatrix} h_x\mathbf{g} & \mathbf{0} \\ \mathbf{0} & h_y\mathbf{g} \\ \mathbf{0} & \mathbf{0} \end{bmatrix}^{\mathrm{T}} \mathbf{C} \begin{bmatrix} h_x\mathbf{g} & \mathbf{0} \\ \mathbf{0} & h_y\mathbf{g} \\ \mathbf{0} & \mathbf{0} \end{bmatrix} \right\rangle$$

$\mathbf{C}$ is the material elasticity matrix and $\langle\ \rangle$ is the integral operator over the element domain.

3. SINGLE-ELEMENT CONSIDERATION

In this section, the isosceles trapezoidal element in Figure 2 is considered. The geometric parameters of the element as defined in equations (1) and (2) are $a_1 = L, a_2 = d, b_3 = h, j_0 = Lh, j_2 = hd$ and $a_3 = b_1 = b_2 = j_1 = 0$. For zero Poisson's ratio, the displacement components

$$u = xy \quad \text{and} \quad u = -x^2/2 \tag{6}$$

represent a pure bending field in which the only non-zero strain is the bending strain ε_x. Repeating MacNeal's test [15], the nodal displacements of the SRI element are prescribed according to equation (6). With equation (4) invoked, the element strains are

$$\varepsilon_x = \frac{h(d + L\eta)}{L + d\eta} \approx h\eta = y, \quad \varepsilon_y = -\frac{Ld}{h}, \quad \gamma_{xy} = 0 \tag{7}$$

For slender beam ($L \gg h$) and d being comparable to h, the error in the element transverse strain ε_y is much larger than the bending strain. Hence, the element strain energy will be erroneous and dominated by the constant transverse strain mode unless the latter is made inadmissible in the element. Unfortunately, this remedy leads to patch test failure [14, 15].

However, practitioners seldom model a problem with only one element. To examine the element accuracy in practical assemblages such as the ones depicted in Figures 3 and 4, it is worthwhile to consider an element with one side fully restrained and apply a bending moment at the other side as shown in Figure 2. The notion behind this is the same as constraint counting in identifying shear and dilatational lockings [21, 22]. In terms of the active nodal d.o.f.s, the constant and non-constant element strains are

$$\varepsilon_c = \frac{1}{4Lh} \begin{bmatrix} h & h & 0 & 0 \\ 0 & 0 & -L & L \\ -L & L & h & h \end{bmatrix} \begin{Bmatrix} u_2 \\ u_3 \\ v_2 \\ v_3 \end{Bmatrix} \tag{8a}$$

$$\varepsilon_{nc} = \frac{1}{4Lh(L + \eta d)} \begin{bmatrix} -h\eta(L + d) & h\eta(L - d) & 0 & 0 \\ 0 & 0 & -L\xi(L + d) & L\xi(L - d) \\ 0 & 0 & 0 & 0 \end{bmatrix} \begin{Bmatrix} u_2 \\ u_3 \\ v_2 \\ v_3 \end{Bmatrix} \tag{8b}$$
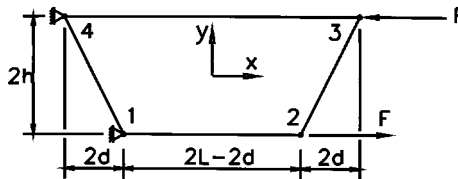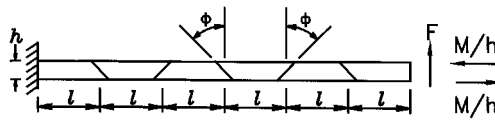

Figure 2. An isosceles trapezoidal element

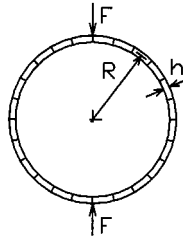Figure 3. Cantilever modelled by trapezoidal mesh; in MacNeal's setting, $\ell = 1$, $h = 0{\cdot}2$, $\phi = 45°$

Figure 4. The pinched ring problem; Poisson's ratio $= 0{\cdot}3$

It can be seen that the magnitudes of the largest entries in the rows of the above strain–displacement matrices pertinent to ε_x, ε_y and γ_{xy} are in the ratio of $h:L:L$. Hence, both ε_y and γ_{xy} are parasitic for $L \gg h$ and the constraints are

$$v_3 - v_2 = 0, \quad (L - d)v_3 - (L + d)v_2 = 0, \quad L(u_3 - u_2) - h(v_2 + v_3) = 0 \quad \text{for} \quad h/L \to 0 \quad (9)$$

The first constraint imposes the equality condition $v_2 = v_3$ which leads to an under-estimation of the deflection due to Poisson's ratio coupling of the normal strain components. A state of plane strain instead of plane stress will be incorrectly predicted. This phenomenon is sometimes known as 'thickness locking' [23]. It disappears when Poisson's ratio vanishes.

Provided that d is not equal to zero, the second constraint after being simplified by the first one becomes

$$v_2 + v_3 = 0 \quad (10)$$

which is much more detrimental than $v_2 = v_3$. Hence, the second constraint which corresponds to the transverse bending mode is the dominant source of 'trapezoidal locking' in practical analyses. To further elucidate this point, the sum of the constant strain constituent given in equation (4) and the following scaled non-constant strain constituent is employed to compute the element stiffness for the test in Figure 2:

$$\boldsymbol{\varepsilon}_{nc} = \begin{bmatrix} h_x \mathbf{g} & \mathbf{0} \\ \mathbf{0} & \mu h_y \mathbf{g} \\ \mathbf{0} & \mathbf{0} \end{bmatrix} \begin{Bmatrix} \mathbf{u}^e \\ \mathbf{v}^e \end{Bmatrix}$$

$$= \frac{1}{4Lh(L + \eta d)} \begin{bmatrix} -h\eta(L + d) & h\eta(L - d) & 0 & 0 \\ 0 & 0 & -\mu L\xi(L + d) & \mu L\xi(L - d) \\ 0 & 0 & 0 & 0 \end{bmatrix} \begin{Bmatrix} u_2 \\ u_3 \\ v_2 \\ v_3 \end{Bmatrix} \quad (11)$$

K. Y. SZE

in which μ is the scaling factor for the transverse bending mode. The geometric parameters L and h are now fixed at 1 and 1/10, respectively. Moreover, Poisson's ratio is set to zero so as to avoid 'thickness locking'. d/h and μ are varied in this test. As the differences between the predicted vertical deflections at nodes 2 and 3 are less than 5 in all cases, only the ones at node 3 are plotted as in Figure 5. The element predictions are exact for $d = 0$. Apparently, 'trapezoidal locking' in practical analysis can be circumvented when μ is sufficiently small.

Though the above selectively scaled SRI element is free from 'trapezoidal locking' in practical analysis, it has several shortcomings: (a) it is not frame invariant, (b) it exhibits 'dilatational locking', (c) it exhibits 'thickness locking' and (d) when μ is taken to be zero, the element is rank deficient.

4. FIVE-BETA HYBRID-STRESS ELEMENTS

Hellinger–Reissner functional is often used to construct the hybrid stress finite element models [1, 2]. The elementwise form of the functional is given as

$$\Pi_{HR}^{e} = \left\langle -\tfrac{1}{2}\boldsymbol{\sigma}^{T}\mathbf{C}^{-1}\boldsymbol{\sigma} + \boldsymbol{\sigma}^{T}\boldsymbol{\varepsilon} \right\rangle \tag{12}$$

in which $\boldsymbol{\sigma}$ is the assumed stress, $\boldsymbol{\varepsilon}$ is the displacement-derived and the load potential is ignored for simplicity. The assumed stresses for Pian and Sumihara's element [2], abbreviated as PS, and Yuan, Huang and Pian's element [4], abbreviated as YHP, can be expressed as

$$\boldsymbol{\sigma} = \{\sigma_x, \sigma_y, \tau_{xy}\}^{T} = \boldsymbol{\beta}_{c} + \mathbf{P}_{nc}\boldsymbol{\beta}_{nc} = [\mathbf{I}_3, \mathbf{P}_{nc}] \begin{Bmatrix} \boldsymbol{\beta}_{c} \\ \boldsymbol{\beta}_{nc} \end{Bmatrix} \tag{13}$$

where

$$\mathbf{P}_{nc} = \begin{bmatrix} a_1 a_1 \eta' & a_3 a_3 \xi' \\ a_1 b_1 \eta' & a_3 b_3 \xi' \\ b_1 b_1 \eta' & b_3 b_3 \xi' \end{bmatrix}$$

is the non-constant stress shape function matrix; $\boldsymbol{\beta}_{c}$ and $\boldsymbol{\beta}_{nc}$ are the vectors of coefficients for the constant and non-constant stress modes.

In the non-constant stress shape function matrix $\mathbf{P}_{nc}$

$$\xi' = \xi - \frac{j_1}{3j_0} \quad \text{and} \quad \eta' = \eta - \frac{j_2}{3j_0} \quad \text{for PS} \tag{14a}$$

$$\xi' = \xi + \frac{j_2}{j_0}\xi\eta - \frac{j_1}{3j_0} \quad \text{and} \quad \eta' = \eta + \frac{j_1}{j_0}\xi\eta - \frac{j_2}{3j_0} \quad \text{for YHP} \tag{14b}$$

In References 2 and 4, the constant terms in ξ' and η' are absent. However, the assumed stress spaces and thus the element models remain intact with the included constant terms which aim to orthogonalize the constant and non-constant stress modes such that the integral of $\mathbf{P}_{nc}$ is equal to zero. It can be shown that the two non-constant stress modes are bending in nature and their neutral axes are essentially parallel to the ξ- and η-axis [2, 4]. Moreover, the stresses of PS are in pointwise homogeneous equilibrium only if the element is a parallelogram. On the other hand, the assumed stresses of YHP are in pointwise equilibrium regardless of the element shape [4].

With the assumed stress in equation (14) and the displacement-derived strain in equation (3), equation (12) becomes

$$\Pi_{HR}^e = -\frac{1}{2}\begin{Bmatrix}\boldsymbol{\beta}_c \\ \boldsymbol{\beta}_{nc}\end{Bmatrix}^T \begin{bmatrix} 4j_0\mathbf{C}^{-1} & \mathbf{0}_{3\times 2} \\ \mathbf{0}_{2\times 3} & \langle \mathbf{P}_n^T\mathbf{C}^{-1}\mathbf{P}_n\rangle \end{bmatrix}\begin{Bmatrix}\boldsymbol{\beta}_c \\ \boldsymbol{\beta}_{nc}\end{Bmatrix} + 4j_0\boldsymbol{\beta}_c^T\mathbf{B}_c\begin{Bmatrix}\mathbf{u}^e \\ \mathbf{v}^e\end{Bmatrix} + \boldsymbol{\beta}_{nc}^T\begin{bmatrix}\mathbf{G}_1 \\ \mathbf{G}_2\end{bmatrix}\begin{Bmatrix}\mathbf{u}^e \\ \mathbf{v}^e\end{Bmatrix} \quad (15)$$

where

$$\mathbf{G}_1 = [a_1a_1 \quad a_1b_1 \quad b_1b_1]\langle \eta'\mathbf{B}_{nc}\rangle \quad \text{and} \quad \mathbf{G}_2 = [a_3a_3 \quad a_3b_3 \quad b_3b_3]\langle \xi'\mathbf{B}_{nc}\rangle$$

are the leverage row vectors. Variation of Π_{HR}^e with respect to $\boldsymbol{\beta}$'s enforces [1]

$$\boldsymbol{\beta}_c = \mathbf{C}\mathbf{B}_c\begin{Bmatrix}\mathbf{u}^e \\ \mathbf{v}^e\end{Bmatrix} \quad \text{and} \quad \langle \mathbf{P}_{nc}^T\mathbf{C}^{-1}\mathbf{P}_{nc}\rangle\boldsymbol{\beta}_{nc} = \begin{bmatrix}\mathbf{G}_1 \\ \mathbf{G}_2\end{bmatrix}\begin{Bmatrix}\mathbf{u}^e \\ \mathbf{v}^e\end{Bmatrix} \quad (16)$$

With $\boldsymbol{\beta}$'s eliminated from Π_{HR}^e

$$\Pi_{HR}^e = \frac{1}{2}\begin{Bmatrix}\mathbf{u}^e \\ \mathbf{v}^e\end{Bmatrix}^T \mathbf{k}\begin{Bmatrix}\mathbf{u}^e \\ \mathbf{v}^e\end{Bmatrix} \quad (17)$$

in which

$$\mathbf{k} = 4j_0\mathbf{B}_c^T\mathbf{C}\mathbf{B}_c + \begin{bmatrix}\mathbf{G}_1 \\ \mathbf{G}_2\end{bmatrix}^T \langle \mathbf{P}_{nc}^T\mathbf{C}^{-1}\mathbf{P}_{nc}\rangle^{-1}\begin{bmatrix}\mathbf{G}_1 \\ \mathbf{G}_2\end{bmatrix}$$

is the element stiffness matrix. It is possible to ignore the two off-diagonal terms in the flexibility matrix $\langle \mathbf{P}_{nc}^T\mathbf{C}^{-1}\mathbf{P}_{nc}\rangle$ without jeopardizing the patch test fulfillment. Extensive numerical experiments indicate that the element accuracy would be virtually unaffected by the diagonalization [3]. Both PS and YHP suffer from 'trapezoidal locking'.

5. SELECTIVE SCALING FOR HYBRID STRESS ELEMENTS

It is well known that shear, membrane and dilatational lockings are due to the improper control of the transverse shear, membrane and dilatational energies, respectively [21, 22]. In hybrid stress elements, these lockings can be alleviated by reducing the number of parasitic stress modes, namely, the transverse shear, membrane and dilatational stress modes, respectively. If the number of parasitic stress modes cannot be reduced due to element rank consideration, locking can still be alleviated by the selective scaling technique [24]. In applying the technique, positive non-dimensional parameters are used to scale some selected leverage row vectors pertinent to the parasitic stress modes. A point to note is that the leverage row vectors arising from the constant stress modes cannot be scaled, or the element model would fail the patch test [3, 24].

With the bending stress modes given in equation (13) and the observation in Section 3, 'trapezoidal locking' in practical analyses can be overcome by scaling $\mathbf{G}_2$ when ξ-axis of the element is aligned with the neutral axis of the applied bending stress and vice versa. Nevertheless, it is not convenient for the users to align the neutral axis with any specific natural co-ordinate axis. Moreover, Figure 5 and the identification of the constraints in equation (9) indicate that the severity of 'trapezoidal locking' in practical analysis increases with d/h and L/h whereas the 'locking' disappears when d/h vanishes. This section aims to devise intelligent scaling parameters for $\mathbf{G}_1$ and $\mathbf{G}_2$ that take into account the element distortion, element aspect ratio and the
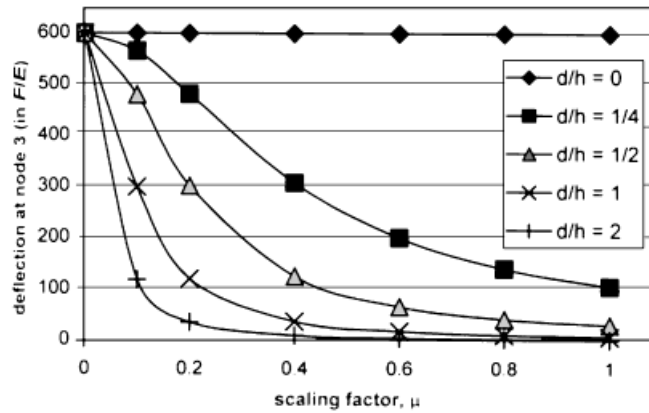
Figure 5. The predicted vertical deflection at node 3 for various d and h ratios, see Figure 2

randomness of the neutral axis of the applied bending stress with respect to the natural co-ordinate axes.

Returning to the isosceles trapezoidal element in Figure 2, when the connectivity is defined in such a way that the ξ-axis is parallel to the two parallel sides of the element, it can be shown that

$$\left(\frac{L}{h}\right)^2 = \frac{a_1^2 + b_1^2}{a_3^2 + b_3^2}, \quad \left(\frac{d}{h}\right)^2 = \left(\frac{j_2}{j_0}\right)^2 \frac{a_1^2 + b_1^2}{a_3^2 + b_3^2} \quad \text{and} \quad \left(\frac{L}{h}\right)^2 \tan^2\phi = \left(\frac{a_1^2 + b_1^2}{a_3^2 + b_3^2}\frac{j_2}{j_0}\right)^2 \quad (18a)$$

On the other hand, when η-axis is parallel to the two parallel sides

$$\left(\frac{L}{h}\right)^2 = \frac{a_3^2 + b_3^2}{a_1^2 + b_1^2}, \quad \left(\frac{d}{h}\right)^2 = \left(\frac{j_1}{j_0}\right)^2 \frac{a_3^2 + b_3^2}{a_1^2 + b_1^2} \quad \text{and} \quad \left(\frac{L}{h}\right)^2 \tan^2\phi = \left(\frac{a_3^2 + b_3^2}{a_1^2 + b_1^2}\frac{j_2}{j_0}\right)^2 \quad (18b)$$

After some numerical experiments, the following scaled invariant formulation is arrived:

$$\mathbf{k}_\kappa = 4j_0\mathbf{B}_c^{\mathrm{T}}\mathbf{C}\mathbf{B}_c + \begin{bmatrix} \chi_1\mathbf{G}_1 \\ \chi_2\mathbf{G}_2 \end{bmatrix}^{\mathrm{T}} \langle\mathbf{P}_n^{\mathrm{T}}\mathbf{C}^{-1}\mathbf{P}_n\rangle^{-1} \begin{bmatrix} \chi_1\mathbf{G}_1 \\ \chi_2\mathbf{G}_2 \end{bmatrix} \quad (19a)$$

and

$$\boldsymbol{\beta}_c = \mathbf{C}\mathbf{B}_c\begin{Bmatrix}\mathbf{u}^e \\ \mathbf{v}^e\end{Bmatrix} \quad \text{and} \quad \boldsymbol{\beta}_{nc} = \langle\mathbf{P}_{nc}^{\mathrm{T}}\mathbf{C}^{-1}\mathbf{P}_{nc}\rangle^{-1}\begin{bmatrix}\chi_1\mathbf{G}_1 \\ \chi_2\mathbf{G}_2\end{bmatrix}\begin{Bmatrix}\mathbf{u}^e \\ \mathbf{v}^e\end{Bmatrix} \quad (19b)$$

in which

$$\frac{1}{\chi_1} = \sqrt{1 + \kappa\left(\frac{a_3^2 + b_3^2}{a_1^2 + b_1^2}\frac{j_1}{j_0}\right)^2} \quad \text{and} \quad \frac{1}{\chi_2} = \sqrt{1 + \kappa\left(\frac{a_1^2 + b_1^2}{a_3^2 + b_3^2}\frac{j_2}{j_0}\right)^2}$$

In the above expressions, $\kappa > 0$ is a non-dimensional positive scalar and both χ_i's are equal to unity when the Jacobian determinant is a constant, i.e. $j_1 = j_2 = 0$.

6. NUMERICAL EXAMPLES

In this section, popular benchmark problems will be studied by a number of five-beta hybrid stress element models including:

(1) PS—the model proposed by Pian and Sumihara [2].
(2) YHP—the model proposed by Yuan *et al.* [4].
(3) PS-E—the model proposed by Wu and Cheung [5]; PS-E is formed by including a penalty equilibrium constraint to PS, see the appendix.
(4) PS-ME—a model modified from PS-E that accounts for the dimensional inconsistency of the penalty matrix by multiplying it with j_0, see the appendix.
(5) SPS—the scaled version of PS devised in the present paper, see equation (19).
(6) SYHP—the scaled version of YHP devised in the present paper, see equation (19).

Patch test, *rank test*, *geometric invariance and sensitivity to connectivity numbering*—All the above models pass MacNeal and Harder's patch test [25] and have five non-zero eigenvalues. They have also been tested to be geometric invariant and insensitive to different connectivity numbering schemes by using the single-element test in Reference 26.

MacNeal and Harder's slender cantilever—By fixing the thickness of the cantilever in Figure 3 at 0·2, ℓ and ϕ are varied. The normalized end deflections are computed and listed in Tables I and II. It can be seen that the proposed parametric factors have rendered the accuracy of SPS and SYHP a rather weak function of ℓ/h and d/h. The accuracy increases with increasing κ. PS-E and PS-ME is comparatively more sensitive to the changing geometric parameters.

Table I. Normalized deflections for $\ell/h = 5$ and different ϕ's in the cantilever problem in Figure 3

Element model	End loading	$\tan \phi = 1/4$	$\tan \phi = 1/2$	$\tan \phi = 1$	$\tan \phi = 2$
PS	Moment	0·287	0·117	0·046	0·025
	Shear	0·317	0·133	0·052	0·026
YHP	Moment	0·287	0·117	0·047	0·025
	Shear	0·317	0·133	0·518	0·268
PS-E/PS-ME	Moment	0·949	0·950	0·955	0·965
	Shear	0·950	0·951	0·955	0·962
SPS	Moment	0·486	0·415	0·394	0·387
($\kappa = 50$)	Shear	0·554	0·494	0·476	0·470
SYHP	Moment	0·486	0·416	0·398	0·403
($\kappa = 50$)	Shear	0·554	0·495	0·480	0·486
SPS	Moment	0·860	0·853	0·852	0·851
($\kappa = 500$)	Shear	0·875	0·870	0·868	0·867
SYHP	Moment	0·858	0·854	0·854	0·860
($\kappa = 500$)	Shear	0·874	0·870	0·871	0·875
SPS	Moment	0·983	0·983	0·983	0·983
($\kappa = 5000$)	Shear	0·978	0·978	0·978	0·978
SYHP	Moment	0·983	0·983	0·983	0·984
($\kappa = 5000$)	Shear	0·979	0·978	0·978	0·979

Table II. Normalized deflections for $\phi = \pi/4$ and different ℓ/h's in the cantilever problem in Figure 3

Element model	End loading	$\ell/h = 1/4$	$\ell/h = 5$	$\ell/h = 10$	$\ell/h = 15$
PS	Moment	0·180	0·046	0·014	0·006
	Shear	0·208	0·052	0·015	0·007
YHP	Moment	0·181	0·465	0·014	0·006
	Shear	0·210	0·518	0·015	0·007
PS-E	Moment	0·999	0·955	0·056	0·379
	Shear	0·994	0·955	0·634	0·257
PS-ME	Moment	0·997	0·955	0·730	0·456
	Shear	0·993	0·955	0·762	0·526
SPS	Moment	0·444	0·394	0·387	0·385
($\kappa = 50$)	Shear	0·521	0·476	0·469	0·498
SYHP	Moment	0·464	0·398	0·388	0·385
($\kappa = 50$)	Shear	0·542	0·480	0·470	0·498
SPS	Moment	0·859	0·852	0·851	0·851
($\kappa = 500$)	Shear	0·877	0·868	0·867	0·867
SYHP	Moment	0·871	0·854	0·852	0·851
($\kappa = 500$)	Shear	0·888	0·871	0·868	0·867
SPS	Moment	0·983	0·983	0·983	0·983
($\kappa = 5000$)	Shear	0·981	0·978	0·978	0·978
SYHP	Moment	0·985	0·983	0·983	0·983
($\kappa = 5000$)	Shear	0·983	0·978	0·978	0·978

Table III. Normalized tip deflections for the pinched ring problem, see Figure 4

	$R/h = 60$	$R/h = 100$	$R/h = 500$
PS	0·715	0·504	0·042
YHP	0·715	0·504	0·042
PS-E	0·944	0·942	0·869
PS-ME	0·943	0·938	0·514
SPS ($\kappa = 500$)	0·945	0·945	0·945
SYHP ($\kappa = 500$)	0·945	0·945	0·945
SPS ($\kappa = 5000$)	0·947	0·947	0·946
SYHP ($\kappa = 5000$)	0·947	0·947	0·946
Reference solutions [27]	$0·8928P(R/h)^3/E$	$0·8927P(R/h)^3/E$	$0·8927P(R/h)^3/E$

Pinched ring—As experienced practitioners always model a straight beam with rectangular mesh, a real nuisance of 'trapezoidal locking' is in arch analyses. For the one in Figure 4, a quarter of the ring is modelled by six elements. The normalized ring deflections under the pinching forces are listed in Table III and Figure 5. Only, SPS and SYHP are insensitive to the aspect ratio. Higher accuracy can be obtained by employing more elements.

Plane wedge subjected to end shear—This problem is modelled by a 4×4 mesh in Figure 6. The best known solutions for maximum principal stress at A, minimum principal stress at B and
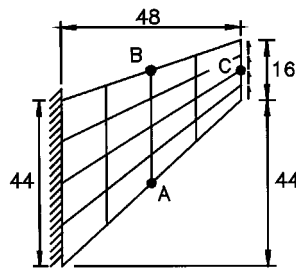
Figure 6. Plane wedge subjected to unit end shear force

Table IV. Normalized deflections and stresses for plane wedge subjected to end shear, see Figure 6

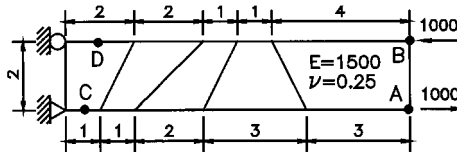| Element model	2 × 2 mesh			4 × 4 mesh		
	σ_A (max)	σ_B (min)	v_C	σ_A (max)	σ_B (min)	v_C
PS	0·858	0·907	0·884	1·019	1·103	0·963
YHP	0·905	0·843	0·893	1·028	1·104	0·964
PS-E	0·762	0·665	1·084	0·948	0·884	1·008
PS-ME	0·741	0·519	1·257	0·924	0·822	1·035
SPS ($\kappa = 500$)	0·965	0·747	1·102	1·030	1·035	0·992
SYHP ($\kappa = 500$)	1·020	0·681	1·108	1·039	1·042	0·993
SPS ($\kappa = 5000$)	0·885	0·600	1·227	0·997	0·935	1·023
SYHP ($\kappa = 5000$)	0·915	0·563	1·228	1·000	0·944	1·023

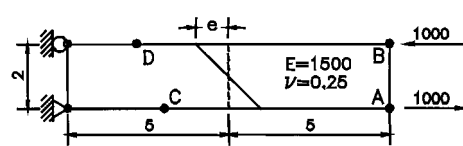
Figure 7. Five-element cantilever subjected end moment

Figure 8. The same cantilever as in Figure 5 modelled by two elements

vertical deflection at C are 0·236, −0·201 and 23·9, respectively. The corresponding normalized predictions are given in Table IV. Overall speaking, the four-scaled models are most accurate.

Five-element cantilever subjected to end moment—The vertical deflections at nodes A and B as well as the stress components at points C and D in the 2×10 cantilever shown in Figure 7 are listed in Table V. Besides PS and YHP, all other models yield accurate results.

Two-element cantilever subjected to end moment—The same cantilever in the previous example is here modelled by two elements with their distortion specified by the length 'e' as shown in Figure 8. When 'e' is equal to zero, all models yield exact displacement and stress predictions. For the examined range of 'e', all the penalty and scaled models yield very accurate stresses. For instance, the bending stresses at points C and D are always within 1 per cent error. The interesting quantities to note are the vertical displacements at nodes A and B denoted as v_A and v_B in

Table V. Predicted tip deflections and stresses in the five-element cantilever, see Figure 7

Element model	v_A (bot)	v_B (up)	σ_{xC} (b)	σ_{yC}	τ_{xyC}	σ_{xD} (u)	σ_{yD}	τ_{xyD}
PS	96·18	94·01	3007	− 18·74	− 9·37	− 3014	− 18·74	− 9·37
YHP	96·50	94·34	3006	− 17·22	− 8·61	− 3013	− 17·22	− 8·61
PS-E	99·88	97·57	3000	0·41	0·20	− 3000	0·41	0·20
PS-ME	100·36	97·56	3000	0·02	0·01	− 3000	0·02	0·01
SPS ($\kappa = 500$)	101·79	97·33	3001	− 3·49	− 1·75	− 3003	− 3·49	− 1·75
SYHP ($\kappa = 500$)	101·78	97·37	3001	− 2·86	− 1·43	− 3002	− 2·86	− 1·43
SPS ($\kappa = 5000$)	102·10	97·54	3000	− 0·45	− 0·23	− 3000	− 0·45	− 0·23
SYHP ($\kappa = 5000$)	102·10	97·54	3000	− 0·37	− 0·18	− 3000	− 0·37	− 0·18
Analytical	100	100	3000	0	0	− 3000	0	0

Table VI. Predicted tip deflections in the two-element cantilever, see Figure 8; exact deflection = 100

Element model	$e = 1$ v_A/v_B	$e = 2$ v_A/v_B	$e = 3$ v_A/v_B	$e = 4$ v_A/v_B	$e = 4\cdot9$ v_A/v_B
PS	67·9/62·9	63·1/55·0	67·2/54·8	70·0/63·0	70·3/49·8
YHP	68·1/63·4	65·1/56·5	71·4/57·6	78·0/57·9	83·7/56·9
PS-E	109·6/99·7	120·5/99·7	132·9/99·8	147·7/99·8	163.6/99·8
PS-ME	110·0/100·0	120·8/100·0	133·2/100·0	148·0/100·0	164·0/100·0
SPS ($\kappa = 500$)	110·0/100·0	120·5/99·7	132·7/99·6	147·1/99·5	162·6/99·3
SYHP ($\kappa = 500$)	110·0/100·0	120·5/99·8	132·8/99·7	147·5/99·7	163·3/99·6
SPS ($\kappa = 5000$)	110·0/100·0	120·8/99·8	133·2/100·0	147·9/100·0	163·9/99·9
SYHP ($\kappa = 5000$)	110·0/100·0	120·8/100·0	133·2/100·0	148·0/100·0	164·0/100·0

Table VI. For all the penalty and scaled models, the error in v_A is less than 1 per cent whereas the error in v_B increases with 'e' and becomes 62–64 per cent at $e = 4\cdot9$. The large separation of A and B is the result of reducing the stiffness arising from the transverse bending mode. Nevertheless, the average end deflections of the scaled elements in this problem are consistently more accurate than that of their unscaled counterparts. The cantilever under end shear load is also considered. The accuracy of v_A, v_B, σ_{xC} and σ_{xD} is highly similar to that in the case of end moment loading.

7. CONCLUSIONS

It is found in this paper that the transverse bending mode is the most critical parasitic stress/strain mode that leads to 'trapezoidal locking' in practical analyses. A selective scaling technique similar to the one previously developed in Reference [24] is employed to overcome the deficiency in hybrid-stress elements. The two rows in the leverage matrix arising from the two assumed bending stress modes are scaled by two judiciously devised parameters such that the bending stiffness leading to trapezoidal locking is reduced. Compared to Wu and Cheung's penalty–equilibrium approach, the present scaling method is less sensitive to mesh skewness and is applicable to element models using pointwise equilibrating assumed stress fields such as

Yuan *et al.* model [4]. Though the scaling technique is devised specifically for slender elements, the last three numerical examples indicate that it also improves the accuracy for non-slender elements. It is trivial that similar scaling techniques can be applied to hybrid-strain elements and γ-stabilized elements in which explicit shape functions of the bending modes are available.

APPENDIX

The penalty–equilibrium element model proposed by Wu and Cheung employs the following elementwise functional [5]:

$$\Pi^e = \left\langle -\frac{1}{2}\,\boldsymbol{\sigma}^T\mathbf{C}^{-1}\boldsymbol{\sigma} + \boldsymbol{\sigma}^T\boldsymbol{\varepsilon} - \frac{\alpha}{2E}\,(\mathbf{L}^T\boldsymbol{\sigma})^T(\mathbf{L}^T\boldsymbol{\sigma}) \right\rangle$$

where α is the penalty factor, E is the elastic modules, $\mathbf{L}$ is the differential operator such that $\mathbf{L}^T\boldsymbol{\sigma} = \mathbf{0}$ is the homogenous stress equilibrium condition and the remaining symbols have been introduced in equation (12). With the stress modes of Pian–Sumihara element, written as $\boldsymbol{\sigma} = \mathbf{P}\boldsymbol{\beta}$, the functional can be expressed as

$$\Pi^e = -\frac{1}{2}\,\boldsymbol{\beta}^T\left(\langle \mathbf{P}^T\mathbf{C}^{-1}\mathbf{P}\rangle + \frac{\alpha}{E}\,\mathbf{H}_P\right)\boldsymbol{\beta} + \boldsymbol{\beta}^T\langle \mathbf{P}^T\mathbf{B}\rangle\begin{Bmatrix}\mathbf{u}^e \\ \mathbf{v}^e\end{Bmatrix}$$

where $\mathbf{H}_P = \langle(\mathbf{L}^T\mathbf{P})^T(\mathbf{L}^T\mathbf{P})\rangle$ and $\mathbf{B} = \mathbf{B}_c + \mathbf{B}_{nc}$, see equation (3). By setting the first variation of Π^e with respect to $\boldsymbol{\beta}$ to zero

$$\boldsymbol{\beta} = \left(\langle \mathbf{P}^T\mathbf{C}^{-1}\mathbf{P}\rangle + \frac{\alpha}{E}\,\mathbf{H}_P\right)^{-1}\langle \mathbf{P}^T\mathbf{B}\rangle\begin{Bmatrix}\mathbf{u}^e \\ \mathbf{v}^e\end{Bmatrix} \quad \text{and} \quad \Pi^e = -\frac{1}{2}\begin{Bmatrix}\mathbf{u}^e \\ \mathbf{v}^e\end{Bmatrix}^T\mathbf{k}_\alpha\begin{Bmatrix}\mathbf{u}^e \\ \mathbf{v}^e\end{Bmatrix}$$

in which

$$\mathbf{k}_\alpha = \langle \mathbf{P}^T\mathbf{B}\rangle^T\left(\langle \mathbf{P}^T\mathbf{C}^{-1}\mathbf{P}\rangle + \frac{\alpha}{E}\,\mathbf{H}_P\right)^{-1}\langle \mathbf{P}^T\mathbf{B}\rangle$$

Wu and Cheung chose α to be 10^4 [5]. This model is here abbreviated as PS-E. To the best knowledge of the author, PS-E is the first and only four-node plane element model which passes the patch test and is not plagued by 'trapezoidal locking' in practical analysis. Obviously, this penalty method is not applicable to hybrid-stress elements whose stresses are strictly equilibrating, i.e. $\mathbf{H}_P = \mathbf{0}$.

It can be noted that α in PS-E is not dimensionless. The most trivial way of making α dimensionless is to replace $\mathbf{H}_P$ with $j_0\mathbf{H}_P$. The resulting element will be termed as PS-ME. To have the two models yielding identical results in MacNeal and Harder's slender cantilever problem [25], where j_0 for the elements equals $0\cdot05$, α for PS-ME is taken to be $10^4/j_0 = 2 \times 10^5$.

Int. J. Numer. Meth. Engng. **47**, 907–920 (2000)

REFERENCES

1. Pian THH. Derivation of element stiffness matrices by assumed stress distributions. *AIAA Journal* 1964; **2**:1333–1336.
2. Pian THH, Sumihara K. Rational approach for assumed stress finite elements. *International Journal for Numerical Methods in Engineering* 1984; **20**:1685–1695.
3. Sze KY. Efficient formulation of robust hybrid elements using orthogonal stress/strain interpolants and admissible matrix formulation. *International Journal for Numerical Methods in Engineering* 1992; **35**:1–20.
4. Yuan KY, Huang YS, Pian THH. New strategy for assumed stresses for 4-node hybrid stress membrane elements. *International Journal for Numerical Methods in Engineering* 1992; **36**:1747–1763.
5. Wu CC, Cheung YK. On optimization approaches of hybrid stress elements. *Finite Elements in Analysis and Design* 1995; **21**:111–128.
6. Yeo ST, Lee BC. New stress assumption for hybrid stress elements and refined four-node plane and eight-node brick elements. *International Journal for Numerical Methods in Engineering* 1997; **40**:2933–2952.
7. Wilson EL, Taylor RL, Doherty WP, Ghaboussi J. Incompatible displacement models. In *Numerical and Computer Methods in Structural Mechanics*, Fenves S. *et al.* (eds). Academic Press: New York, 1973; 43–57.
8. Taylor RL, Beresford PJ, Wilson EL. A non-conforming element for stress analysis. *International Journal for Numerical Methods in Engineering* 1976; **10**:1211–1219.
9. Simo JC, Rifai MS. A class of mixed assumed strain methods and the method of incompatible modes. *International Journal for Numerical Methods in Engineering* 1990; **29**:1595–1638.
10. Belytschko T, Bachrach WE. Efficient implementation of quadrilaterals with high coarse-mesh accuracy. *Computer Methods in Applied Mechanics and Engineering* 1986; **54**:279–301.
11. Hughes TJR. Generalization of selective integration procedures to anisotropic and nonlinear media. *International Journal for Numerical Methods in Engineering* 1980; **16**:1413–1418.
12. MacNeal RH. Derivation of element stiffness matrices by assumed strain distributions. *Nuclear Engineering and Design* 1982; **70**:3–12.
13. Stolarski HS. On a formulation of the quadrilateral with highly accurate in-plane bending behavior. abstract, *First U.S. National Congress on Computational Mechanics*, July 21–24, Chicago, 1991.
14. MacNeal RH. A theorem regarding the locking of tapered four-noded membrane elements. *International Journal for Numerical Methods in Engineering* 1987; **24**:1793–1799.
15. MacNeal RH. *Finite Elements: Their Design and Performance*. Marcel Dekker: New York, 1994.
16. Allman DJ. A compatible triangular element including vertex rotations for plane elasticity analysis. *Computers and Structures* 1984; **19**:1–8.
17. MacNeal RH. Toward a defect-free four-noded membrane element. *Finite Elements in Analysis and Design* 1989; **5**:31–37.
18. Sze KY, Chen WJ, Cheung YK. An efficient quadrilateral element with drilling degrees of freedom using orthogonal stress modes. *Computers and Structures* 1992; **42**:695–705.
19. Sze KY, Sim YS, Soh AK. A hybrid stress quadrilateral shell element with full rotational D.O.F.s. *International Journal for Numerical Methods in Engineering* 1997; **40**:1785–1800.
20. Bergan PG, Felippa CA. A triangular membrane element with rotational degrees of freedom. *Computer Methods in Applied Mechanics and Engineering* 1985; **50**:25–69.
21. Hughes TJR. *The Finite Element Method—Linear Static and Dynamic Finite Element Analysis*. Prentice-Hall: New Jersey, 1987.
22. Zienkiewicz OC, Taylor RL. *The Finite Element Method*, *vol.* 1-*Basic Formulation and Linear Problems* (4th edn). McGraw-Hill: London, 1989.
23. Hauptmann R, Schweizerhof K. A systematic development of 'solid-shell' element formulations for linear and non-linear analyses employing only displacement degrees of freedom. *International Journal for Numerical Methods in Engineering* 1998; **42**:49–69.
24. Sze KY, Ghali A. An hexahedral element for plates, shells and beams by selective scaling. *International Journal for Numerical Methods in Engineering* 193; **36**:1519–1540.
25. MacNeal RH, Harder RL. A proposed standard set of problems to test finite element accuracy. *Finite Elements in Analysis and Design* 1985; **1**:3–20.
26. Sze KY, Chow CL, Chen W-J. On invariance of isoparametric hybrid elements. *Communications in Applied Numerical Methods* 1992; **8**:385–406.
27. Lee SW, Pian THH. Improvement of plate and shell finite elements by mixed formulations. *AIAA Journal* 1978; **16**:29–34.